AIP | Physics of Fluids

Numerical study on the shape oscillation of an encapsulated microbubble in ultrasound field

Yunqiao Liu, Kazuyasu Sugiyama, Shu Takagi, and Yoichiro Matsumoto

Citation: Phys. Fluids **23**, 041904 (2011); doi: 10.1063/1.3578493
View online: http://dx.doi.org/10.1063/1.3578493
View Table of Contents: http://pof.aip.org/resource/1/PHFLE6/v23/i4
Published by the American Institute of Physics.

Numerical study on the shape oscillation of an encapsulated microbubble in ultrasound field

Yunqiao Liu, Kazuyasu Sugiyama, Shu Takagi,[a)] and Yoichiro Matsumoto
Department of Mechanical Engineering, School of Engineering, The University of Tokyo, 7-3-1 Hongo, Bunkyo-ku, Tokyo 113-8656, Japan

(Received 4 August 2010; accepted 25 March 2011; published online 21 April 2011)

The shape oscillation of an encapsulated microbubble in an ultrasound field is numerically investigated. To predict the nonlinear process, the continuity equation and the Navier–Stokes equation are directly solved by means of a boundary-fitted finite-volume method on an orthogonal curvilinear coordinate system. The mechanics of neo-Hookean membrane is incorporated into the dynamic equilibrium at the bubble surface. The numerical results show that the membrane raises the natural frequency of an encapsulated bubble especially for small bubble, whereas this effect is attenuated as the initial bubble size grows. For a small encapsulated bubble of which the natural frequency is sufficiently higher than the driving frequency, the oscillation is stable, namely, the oscillatory amplitude is small; besides, the radial mode and shape modes are out of resonance so that no deformation emerges. As the bubble becomes larger, the natural frequencies of encapsulated and gas bubbles get closer, leading to the less apparent difference in oscillatory amplitude between them. Furthermore, shape modes of an encapsulated bubble are prone to be induced when twice of the higher-order natural frequency is approximately equal to the frequency of radial mode particularly when the bubble is at radial resonance for which the large-amplitude pulsation enhances the compressive stress developing in the membrane. In contrast, the shape oscillation is less likely to occur for a gas bubble with micrometer size since the surface tension suppresses the developments of nonspherical shape modes. © *2011 American Institute of Physics*. [doi:10.1063/1.3578493]

I. INTRODUCTION

Dynamics of an encapsulated microbubble is practically important to medical ultrasound diagnostics and therapeutics. Ultrasound contrast agent (UCA) in medical sonography is composed of gas-filled microbubbles encapsulated by macromolecular membranes.[1] Due to the compressibility of gas core, the UCA has a high degree of echogenicity and is able to enhance the ultrasound backscatter and to yield high-quality image. The encapsulating membrane protects the gas core from dissolving and withstands bursting under acoustic energy. However, the surface instability induced by the membrane may lead to the breakup of bubbles and shorten the UCA's residence time. In drug delivery system (DDS), encapsulated microbubbles are used to carry drug. When the drug carrier reaches the targeted site, localized ultrasound energy ruptures the encapsulating membrane and releases drug.[2] In this process, the instability of membrane facilitates the bubble breaking up so as to reduce the requisite ultrasound energy and protect the surrounding tissue. No matter in order to avoid the surface instability in UCA or utilize it in DDS, the condition under which the shape instability will take place, as well as the base radial motion, is an important ingredient to be examined.

The shape oscillation of a gas bubble without encapsulation has been well studied.[3–7] Most of the analyses were based on potential flow theory and restricted to a small disturbance to the spherical interface. The equation of amplitude with respect to higher-order shape mode is Mathieu's equation, which characterizes the parametric instability. Such a system is fundamentally linear so that different higher-order modes are uncoupled. The nonlinear mode-coupling phenomenon was simulated by McDougald and Leal[8,9] using boundary-integral technique. The simulation, however, was in the inviscid or weakly viscous limit. In this paper, we will solve the full Navier–Stokes equation on a boundary-fitted grid to investigate the nonlinear stability of the interface.

Since the encapsulating membrane will influence the behavior of a bubble, the study on its dynamics becomes of great interest. Most of the existing studies are confined to the radial motion based on the Rayleigh–Plesset equation with additional terms corresponding to the internal friction within the membrane and the restoring force accounting for membrane stiffness.[10–12] The encapsulated bubble might experience an analogous shape oscillation like the gas bubble exposing in an ultrasound field. The nonspherical oscillation was inferred from a poor consistency in radius-time curves between the experimental result and a Rayleigh–Plesset-like solution for albumin-shelled agents.[13] The Rayleigh–Plesset-like models basically describe radial dynamics. The variants to the Rayleigh–Plesset equation for the shape oscillation are essentially derived for an irrotational flow. These models would be valid when the hydrodynamics is dominated by the kinematic condition associated with the interfacial displacement normal to the bubble surface rather than by the dynamic condition. For the gas bubble, the validity of the Rayleigh–Plesset model has been demonstrated in a number

[a)]Also at Organ and Body Scale Team, CSRP, Riken, 2-1, Hirosawa, Wako-shi, Saitama 351-0198, Japan.

of literatures.[3,4,14] For the encapsulated bubble, however, the dynamic condition must play a significant role in the hydrodynamics since the membrane effect is reflected mainly on the generation of the in-plane stress due to the interfacial displacement tangential to the bubble surface, which accounts for the frictional traction jump between the liquid and gas phases. Therefore, instead of treating only the interfacial motion based on the Rayleigh–Plesset model, we perform direct numerical simulations of the bulk liquid flow around the bubble by means of a boundary-fitted finite-volume approach. We refer to the theory of elastic membrane.[15] Plenty of work based on that theory was developed by Barthès-Biesel's group[16–18] and Pozrikidis' group[19,20] to model the flow-induced deformation of a capsule. We here couple it with the external flow field to investigate the shape oscillation of an encapsulated bubble subjected to an ultrasonic pressure wave.

In the present study, we discuss the stability of an encapsulated microbubble from the viewpoint of resonance relationship and compare with that of gas bubble at the same size. Through investigating the effects of membrane, we try to explain the reason why the encapsulation does not always stabilize the bubble. The paper is organized as follows. In Sec. II, we formulate the governing equations and boundary conditions. In Sec. III, we first reproduce the shape oscillation of a gas bubble as shown in an experimental study[21] to validate our simulation code. Next, seven encapsulated bubbles with initial radii of 1–7 μm are investigated. The interfacial stability is analyzed in terms of spherical harmonics. The resonance phenomenon is explained referring to the relationship among driving frequency and natural frequencies at various order modes. In Sec. IV, we conclude our discussion.

II. PROBLEM FORMULATION

We adopt the boundary-fitted finite-volume method on an orthogonal curvilinear coordinate system. Here we assume axisymmetry, i.e., we do not consider the azimuthal mode in the fluid flow or the interfacial deflection. We use a simulation code developed by Takagi *et al.*,[22,23] which has been well validated for unsteady motions of a deformable rising bubble. In the code, the Navier–Stokes and continuity equations are solved by a SIMPLER algorithm, and the spatial derivatives are approximated by the second-order central difference. At each time step, the boundary-fitted grid is temporally updated as a solution to the covariant Laplace equation to link physical and computational spaces. For a more detailed description, we refer the readers to Ref. 23. The grid and the coordinate system are illustrated in Fig. 1. The boundary-fitted grid is able to precisely describe the shape of bubble since the bubble surface is exactly at one of the boundaries. Additionally, the tangential and normal directions of the bubble surface are parallel with the orthogonal coordinate axes, which makes it straightforward for the expressions of membrane mechanics.

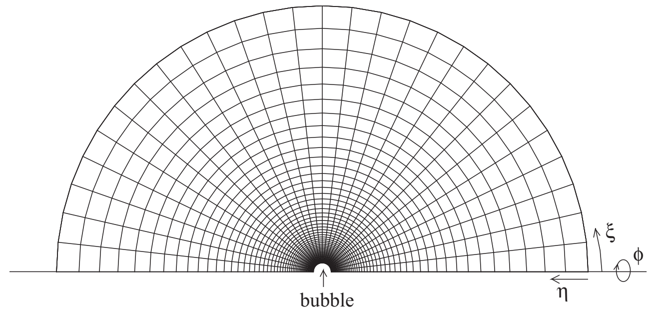

FIG. 1. Grid and coordinate system.

A. Governing equations

The governing equations about the velocity $\mathbf{u}$ and pressure p are expressed in the form of curvilinear coordinates ξ and η. h is the metric coefficient, with the subscripts denoting directions. Under the axisymmetric system, the metric coefficient in azimuthal direction h_ϕ is calculated by the distance from the axis of symmetry.

1. Equation of continuity

The liquid phase is considered as incompressible,

$$\nabla \cdot \mathbf{u} = 0, \tag{1}$$

with a curvilinear coordinate form of

$$\frac{1}{h_\xi h_\eta h_\phi}\left[\frac{\partial}{\partial \xi}(h_\eta h_\phi u_\xi) + \frac{\partial}{\partial \eta}(h_\xi h_\phi u_\eta)\right] = 0. \tag{2}$$

2. Momentum equation

The Navier–Stokes equation without body force is

$$\rho\left(\frac{\partial \mathbf{u}}{\partial t} + \mathbf{u}\cdot\nabla\mathbf{u}\right) = -\nabla p + \mu\nabla\cdot(\nabla\mathbf{u} + \nabla\mathbf{u}^{\mathrm{T}}). \tag{3}$$

In ξ-direction, the above momentum equation is expressed as

$$\begin{aligned}\rho\frac{\partial u_\xi}{\partial t} &+ \frac{\rho}{h_\xi h_\eta h_\phi}\left[\frac{\partial}{\partial \xi}(h_\eta h_\phi u_\xi^2) + \frac{\partial}{\partial \eta}(h_\xi h_\phi u_\xi u_\eta)\right] \\ &= \frac{\mu}{h_\xi h_\eta h_\phi}\left[\frac{\partial}{\partial \xi}\left(\frac{h_\eta h_\phi}{h_\xi}\frac{\partial u_\xi}{\partial \xi}\right) + \frac{\partial}{\partial \eta}\left(\frac{h_\xi h_\phi}{h_\eta}\frac{\partial u_\xi}{\partial \eta}\right)\right] \\ &\quad - \frac{1}{h_\xi}\frac{\partial p}{\partial \xi} + S_\xi,\end{aligned} \tag{4}$$

where S_ξ represents the apparent source term due to the changes in the basis vectors along ξ- and η-directions, i.e.,

$$\begin{aligned}S_\xi = {}& \frac{\rho u_\eta^2}{h_\xi h_\eta}\frac{\partial h_\eta}{\partial \xi} - \frac{\rho u_\xi u_\eta}{h_\xi h_\eta}\frac{\partial h_\xi}{\partial \eta} - \mu\frac{1}{h_\phi^2 h_\xi}\frac{\partial h_\phi}{\partial \xi}\left(\frac{u_\xi}{h_\xi}\frac{\partial h_\phi}{\partial \xi}\right. \\ &\left. + \frac{u_\eta}{h_\eta}\frac{\partial h_\phi}{\partial \eta}\right) + \frac{\mu}{h_\xi h_\eta h_\phi}\left[\frac{\partial}{\partial \xi}\left(u_\eta\frac{h_\phi}{h_\xi}\frac{\partial h_\xi}{\partial \eta}\right)\right. \\ &\left. - \frac{\partial}{\partial \eta}\left(u_\eta\frac{h_\phi}{h_\eta}\frac{\partial h_\eta}{\partial \xi}\right)\right] + \mu\frac{1}{h_\xi h_\eta}\left(\frac{\partial h_\xi}{\partial \eta}\frac{1}{h_\xi}\frac{\partial u_\eta}{\partial \xi}\right. \\ &\left. - \frac{\partial h_\eta}{\partial \xi}\frac{1}{h_\eta}\frac{\partial u_\eta}{\partial \eta}\right) - \mu\frac{u_\xi}{h_\xi^2 h_\eta^2}\left[\left(\frac{\partial h_\xi}{\partial \eta}\right)^2 + \left(\frac{\partial h_\eta}{\partial \xi}\right)^2\right].\end{aligned} \tag{5}$$

The momentum equation in η-direction has an analogous form of

$$\rho\frac{\partial u_\eta}{\partial t}+\frac{\rho}{h_\xi h_\eta h_\phi}\left[\frac{\partial}{\partial \xi}(h_\eta h_\phi u_\xi u_\eta)+\frac{\partial}{\partial \eta}(h_\xi h_\phi u_\eta^2)\right]$$
$$=\frac{\mu}{h_\xi h_\eta h_\phi}\left[\frac{\partial}{\partial \xi}\left(\frac{h_\eta h_\phi}{h_\xi}\frac{\partial u_\eta}{\partial \xi}\right)+\frac{\partial}{\partial \eta}\left(\frac{h_\xi h_\phi}{h_\eta}\frac{\partial u_\eta}{\partial \eta}\right)\right]$$
$$-\frac{1}{h_\eta}\frac{\partial p}{\partial \eta}+S_\eta, \tag{6}$$

where S_η is the one in which ξ and η of Eq. (5) are interchanged.

Since the grid is updated every time step, the time derivative includes terms related to the grid movement and the basis change with time. The time derivative of u_ξ is treated as

$$\frac{\partial u_\xi}{\partial t}=\frac{\partial u_\xi}{\partial \tau}+u_\eta\left(\frac{y_\xi}{h_\xi}\right)^{-1}\frac{\partial}{\partial \tau}\left(\frac{x_\xi}{h_\xi}\right)-\frac{\partial x}{\partial \tau}\left[\frac{1}{h_\xi h_\eta}\left(y_\eta\frac{\partial u_\xi}{\partial \xi}\right.\right.$$
$$\left.\left.-y_\xi\frac{\partial u_\xi}{\partial \eta}\right)\right]-\frac{\partial y}{\partial \tau}\left[\frac{1}{h_\xi h_\eta}\left(-x_\eta\frac{\partial u_\xi}{\partial \xi}+x_\xi\frac{\partial u_\xi}{\partial \eta}\right)\right]$$
$$-\frac{\partial x}{\partial \tau}\left[\frac{u_\eta}{h_\xi h_\eta}\left(\frac{y_\eta}{h_\eta}\frac{\partial h_\xi}{\partial \eta}+\frac{y_\xi}{h_\xi}\frac{\partial h_\eta}{\partial \xi}\right)\right]$$
$$-\frac{\partial y}{\partial \tau}\left[\frac{u_\eta}{h_\xi h_\eta}\left(\frac{x_\eta}{h_\eta}\frac{\partial h_\xi}{\partial \eta}+\frac{x_\xi}{h_\xi}\frac{\partial h_\eta}{\partial \xi}\right)\right]. \tag{7}$$

The time derivative of u_η has an analogous modification.

3. Equation of state

We assume that the gas pressure inside the bubble has a uniform distribution, which is justified as long as the Mach number of the bubble wall motion is sufficiently smaller than unity.[24] In the present simulation, the Mach number, evaluated for a micrometer-size bubble driven at the frequency of megahertz (a common condition for UCA or drug carrier) and with respect to the gas speed of sound, is less than 0.003, indicating that the assumption of uniform gas pressure is reasonable. The gas pressure p_g is determined from a polytropic gas model. As indicated by Plesset and Hsieh,[25] the thermodynamic behavior of a gas bubble in a high-frequency oscillating pressure field may be isothermal rather than adiabatic. Prosperetti[26] further provided a quantitative method to judge the polytropic condition. The thermal penetration length $(\chi/\omega)^{1/2}$ was considered, where χ is the thermal diffusivity [equal to 2.2160×10^{-5} $\mathrm{m^2/s}$ for air under normal condition (1 atm and 300 K)] and ω is the inverse of characteristic time. If the thermal penetration length is larger than the averaged radius of bubble, the pressure variation can be approximated as isothermal. This is true with regard to the characteristic length and frequency in the present study. Hence, we consider the isothermal procedure in this study,

$$p_g V = p_{g0}V_0, \tag{8}$$

where V is the bubble's volume and the subscript 0 represents the initial state.

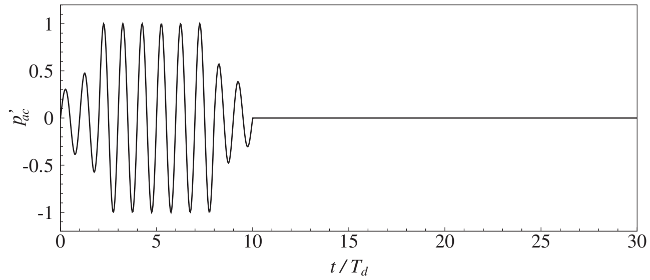

FIG. 2. Applied acoustic pressure.

B. Boundary conditions

1. Oscillatory pressure in the far field

The transmit ultrasound is expressed by a pressure pulse and imposed in the far field. For the sake of a comparison in Sec. III A, we select the form of pressure pulse as that chosen in the experiment done by Versluis *et al.*[21] One pressure pulse consists of a burst of ten-cycle sinusoidal waves, characterized by a dimensionless amplitude ϵ and driving period T_d. The first and last two cycles are modified by the Gaussian envelope. In Eqs. (9) and (10), p_{st} and p_{ac} are the ambient static pressure and the applied acoustic pressure, respectively. Figure 2 shows the normalized applied acoustic pressure pulse p'_{ac}.

$$p_\infty = p_{st}+p_{ac}, \tag{9}$$

$$p_{ac}=p'_{ac}\cdot\epsilon p_{st}. \tag{10}$$

2. Force balances at the bubble surface

The normal and tangential force balances at the bubble surface are derived from the traction jump across the membrane, in which the viscous friction, the surface tension at the gas-liquid interface, and the membrane stress are considered,

$$\mathbf{n}\cdot(-p_l\mathbf{I}+2\mu\mathbf{E})=\mathbf{n}\cdot(-p_g\mathbf{I})+(\gamma\nabla\cdot\mathbf{n})\mathbf{n}+\mathbf{F}, \tag{11}$$

where $\mathbf{n}$ denotes the unit normal vector pointing outward to liquid, $\mathbf{I}$ the unit tensor, $\mathbf{E}$ the strain rate tensor, γ the surface tension, and $\mathbf{F}$ the membrane stress. We assume the water and air system under the atmospheric pressure. The viscosity of gas is negligibly smaller than that of liquid. We project Eq. (11) to the normal direction and obtain the normal force balance,

$$-p_l+2\mu e_{\eta\eta}=-p_g+\gamma(\kappa_s+\kappa_\phi)+F_n, \tag{12}$$

where F_n denotes the normal membrane stress and $e_{\eta\eta}$ is the normal component of the strain rate tensor $\mathbf{E}$,

$$e_{\eta\eta}=\frac{1}{h_\eta}\frac{\partial u_\eta}{\partial \eta}+\frac{u_\xi}{h_\eta h_\xi}\frac{\partial h_\eta}{\partial \xi}. \tag{13}$$

Similarly, we project Eq. (11) to the tangential direction and obtain the tangential force balance,

$$2\mu e_{\eta\xi}=\mu\left[\frac{h_\xi}{h_\eta}\frac{\partial}{\partial \eta}\left(\frac{u_\xi}{h_\xi}\right)+\frac{h_\eta}{h_\xi}\frac{\partial}{\partial \xi}\left(\frac{u_\eta}{h_\eta}\right)\right]=F_t, \tag{14}$$

where F_t denotes the tangential membrane stress. On the basis of the theory of elastic membrane, $\mathbf{F}$ is derived by the

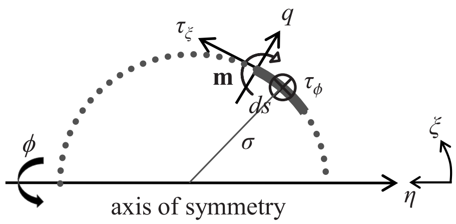

FIG. 3. The elastic tensions and bending moment developing on a patch of membrane.

surface divergence of the elastic tension tensors on a patch of the membrane, two components of which F_n and F_t are written as

$$F_n = \kappa_\xi \tau_\xi + \kappa_\phi \tau_\phi - \frac{1}{h_\xi h_\phi}\frac{\partial}{\partial \xi}(h_\phi q), \quad (15)$$

$$F_t = -\left[\frac{\partial \tau_\xi}{h_\xi \partial \xi} + \frac{1}{h_\xi h_\phi}\frac{\partial h_\phi}{\partial \xi}(\tau_\xi - \tau_\phi) + \kappa_\xi q\right], \quad (16)$$

where τ_ξ and τ_ϕ are the principal in-plane tensions and q is the transverse shear tension (see Fig. 3). q is obtained from a torque balance in terms of the bending moments m_ξ and m_ϕ as follow:

$$q = \frac{1}{h_\phi h_\xi}\frac{\partial h_\phi}{\partial \xi}\left[\frac{\partial}{\partial h_\phi}(h_\phi m_\xi) - m_\phi\right]. \quad (17)$$

C. Constitutive laws for encapsulating membrane

After establishing the membrane mechanics model, we proceed to specify the membrane material in order to connect the in-plane stress of the membrane to its strain. For this purpose, we should find a constitutive law to approximate the physical behavior of a real material. One of the simplest constitutive models is well-known Hooke's law, which describes the linear relationship between stress and strain. However, since Hooke's law assumes an infinitesimal displacement, its linearity restricts the reversibility in shape when the deformation is large. Therefore, we consider hyperelastic materials, for which the surface energy function is defined as a function of the surface Green–Lagrange strain, so as to relate the finite deformation to the in-plane stress. There are two common families in hyperelastic laws, namely, the strain-hardening and strain-softening models. For strain-hardening material, the elastic modulus rises as strain grows; in other words, the natural frequency increases with the oscillatory amplitude. The Skalak law[27] belongs to this kind of material. The strain-softening material behaves in an opposite way to the strain-hardening material. One of the famous strain-softening models is the Mooney–Rivlin law.[28] Sarkar *et al.*[29] predicted a strain-softening behavior in the dilation of the contrast agent Sonazoid when they found an error between their theoretical analysis and experimental results. Accordingly, we adopt the neo-Hookean law, a simple form of the strain-softening Mooney–Rivlin law. The constitutive equations for the in-plane tensions are

$$\tau_\xi = \frac{G_s}{\lambda_\xi \lambda_\phi}\left(\lambda_\xi^2 - \frac{1}{\lambda_\xi^2\lambda_\phi^2}\right), \quad \tau_\phi = \frac{G_s}{\lambda_\xi \lambda_\phi}\left(\lambda_\phi^2 - \frac{1}{\lambda_\xi^2\lambda_\phi^2}\right), \quad (18)$$

where G_s is the surface modulus of elasticity, which characterizes the stiffness of the membrane. λ_s and λ_φ are the principal stretches along the arc-length direction and the azimuthal direction, respectively, expressed by

$$\lambda_\xi = \frac{ds}{ds^R}, \quad \lambda_\phi = \frac{\sigma}{\sigma^R}, \quad (19)$$

where the superscript R denotes the reference state.

The constitutive equations for the bending moments are given by a linear model with respect to the principal curvatures,

$$m_\xi = G_b(\kappa_\xi - \kappa_\xi^R), \quad m_\phi = G_b(\kappa_\phi - \kappa_\phi^R), \quad (20)$$

where G_b is the bending modulus, characterizing the bending resistance.

III. RESULTS AND DISCUSSION

In this section, we will first present the shape oscillation of a gas bubble without encapsulating membrane and compare the results with an experimental observation to validate the numerical computation. Following that we will study the effects of membrane on the stability of the bubble surface. Seven cases, with initial radii from 1 to 7 μm, will be investigated. We assume the surrounding liquid as water, with density $\rho = 1\times 10^3$ kg/m^3 and viscosity $\mu = 0.001$ kg/ms. The ambient static pressure p_{st} is set as 1×10^5 Pa, and the dimensionless driving amplitude $\epsilon = 0.8$.

A. Gas bubble

First we consider a gas bubble exposing in the ultrasound field. In this case, the bubble is purely subjected to surface tension, that is, standard Laplace's law [$F_n=0$ in Eq. (12)] and the free-slip condition [$F_t=0$ in Eq. (14)]. We set the bubble initial radius as 30 μm and the frequency of driving acoustic pressure as 130 kHz according to the experiment performed by Versluis *et al.*[21]

We expand the bubble's shape in terms of the Legendre polynomials,

$$R(\theta) = R_0 + \sum_{k=0}^{\infty} a_k P_k(\cos\theta), \quad (21)$$

where k indicates the mode order: $k=0$ represents the radial mode and $k\geq 2$ denotes the shape modes. $k=1$ relates to the translation of the bubble without deformation, and we do not discuss it in this paper. Actually we find that the translation of bubble center is quite small (less than $10^{-5}R_0$) in the following simulations, implying that the neglecting of the first-order mode is reasonable though it is allowed. The amplitude with respect to specific mode a_k is given by

$$a_k = \frac{2k+1}{2}\int_0^{\pi} R(\theta)P_k(\cos\theta)\sin\theta d\theta. \quad (22)$$

The evolutions of various modes are plotted in Fig. 4. At the beginning, the oscillation is at a purely radial mode. After

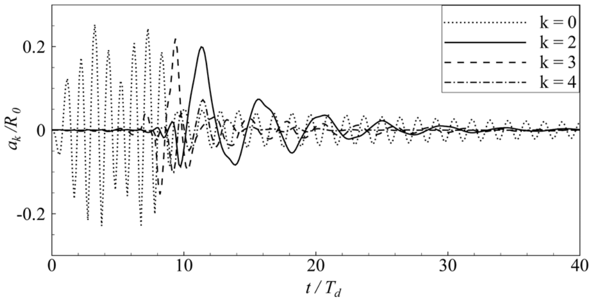

FIG. 4. Amplitudes of different modes of a gas bubble (R_0=30 μm) vs time. Dotted line: k=0; solid line: k=2; dashed line: k=3; and dashed-dotted line: k=4.

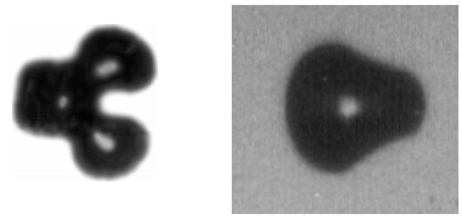

FIG. 6. Snapshots of the third-order shape mode (Ref. 21).

several cycles of large-amplitude pulsation, the surface instability is excited for higher-order modes. With the accumulation of parametric instability, the third-order shape mode becomes obvious, accompanied by a fourth-order mode at smaller amplitude. Subsequently, higher-order modes degrade to second-order mode. After withdrawing the pressure pulse, all the modes are gradually damped due to the viscous effect. In this process of shape oscillation, various order modes are coupled and no obvious demarcation for individual mode exists.

Instantaneous bubble shapes from t=7.25T_d to t=16.75T_d with interval of 0.5T_d are presented in Fig. 5. The third- and second-order preferred shape modes emerge during this stage. Two snapshots of the bubble with the specified radius and driving frequency which were taken by Versluis *et al.*[21] are shown in Fig. 6, from which we also see the third-order shape mode.

The temporal variation of the bubble volume is compared with the solution to the standard Rayleigh–Plesset equation which concerns the radial motion of a spherical bubble. Here, we use an in-house code, in which the Rayleigh–Plesset equation is numerically solved by the fourth-order Runge–Kutta method to temporally update the bubble radius and its time derivative. The comparison is shown in Fig. 7, where the volumetric change is normalized by the initial volume V_0 and the time is normalized by the driving period T_d. The beginning behavior of the present simulation is in good agreement with the Rayleigh–Plesset solution. The emergence of shape oscillation slightly shifts the oscillatory phase. The amplitude of our volume oscillation is smaller, and the damping is faster than that in the Rayleigh–Plesset solution. This implies that the shape oscillation causes energy transfer from the purely radial mode, and thus more kinetic energy is consumed.

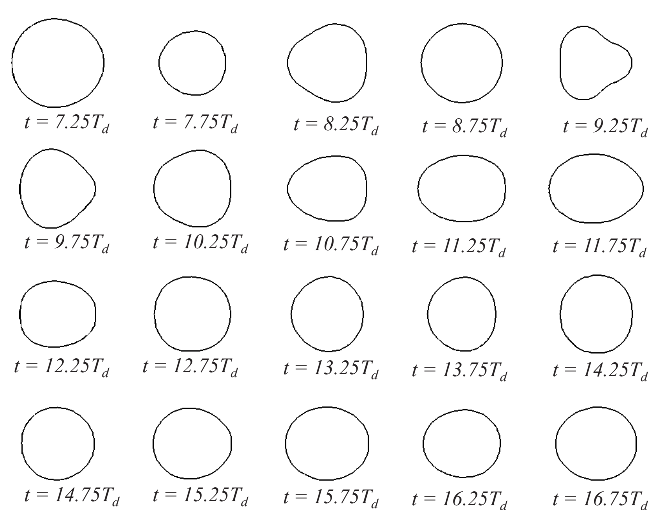

FIG. 5. Instantaneous shapes of a gas bubble (R_0=30 μm) from t=7.25T_d to t=16.75T_d with interval of 0.5T_d.

B. Encapsulated bubble

When used as contrast-enhanced agent or drug carrier, the bubble is encapsulated by membrane which is composed of albumin, galactose, lipid, or polymer. Here we treat the membrane as a neo-Hookean hyperelastic material. For the membrane parameter, the surface elastic modulus G_s is usually estimated by fitting the experimental data with the Church–Hoff model.[11,12,29] The estimated G_s is on the order of 10^{-1} N/m. In the following simulation, we select a relatively small G_s as 0.1 N/m considering that the Church–Hoff model assumes a linear stress-strain relationship which may overestimate the stiffness of the membrane. There are few experimental measurements for bending modulus G_b. The absence of bending resistance would lead to numerical instability physically resulting from buckling under compression.[30] We set therefrom G_b as 2×10^{-13} N m in the guarantee of eliminating numerical instability. The size of encapsulated bubble is on the order of micrometer allowing for safe medical application. We choose bubbles with equilibrium radii from R_0=1 μm to R_0=7 μm with interval of 1 μm. Since surface tension is small when the bubble is encapsulated by a membrane,[1] we drop the surface tension in Eq. (12). The driving frequency of transmit ultrasound is chosen as 1 MHz according to the practical medical application.

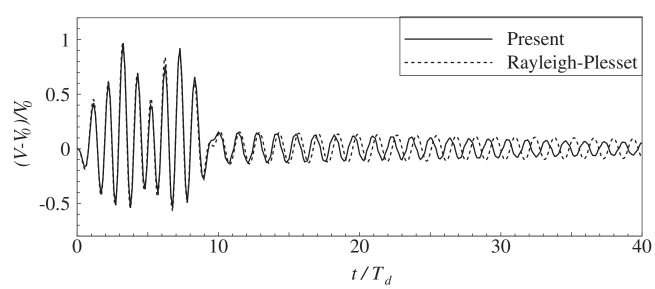

FIG. 7. Change rate of volume vs time of a gas bubble (R_0=30 μm), compared with the Rayleigh–Plesset solution (dashed line).

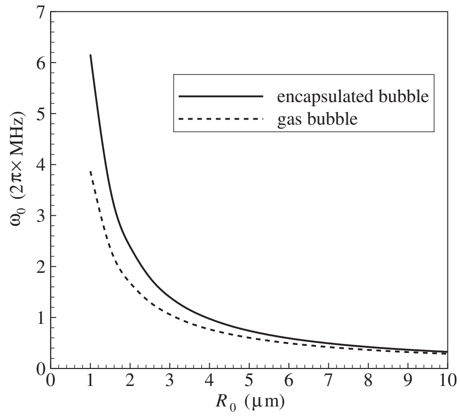

FIG. 8. Natural frequency vs radius for encapsulated bubble (solid line) and gas bubble (dashed line).

First of all, we derive a modified Rayleigh–Plesset equation for the following comparison. Since it restricts to the radial motion, only the normal stress F_n is needed. In the expression of F_n [Eq. (15)], the transverse shear tension q remains zero if no deformation occurs. For the spherical bubble, the curvature is the reverse of instant radius ($\kappa_\xi = \kappa_\phi = 1/R$), and both of the principal stretches λ_ξ and λ_ϕ are calculated by R/R_0. In this way, we obtain the modified Rayleigh–Plesset equation,

$$R\ddot{R} + \frac{3}{2}(\dot{R})^2 = \frac{1}{\rho}\left[p_{g0}\left(\frac{R_0}{R}\right)^3 - p_\infty - \frac{2\gamma}{R} - \frac{4\mu}{R}\dot{R} - 2G_s\frac{R^6 - R_0^6}{R^7}\right]. \tag{23}$$

In order to investigate the natural frequency, we introduce a disturbance to the radius

$$R = R_0[1 + x(t)], \quad \text{with } x(t) \ll 1. \tag{24}$$

Substituting it into Eq. (23), we obtain a linear oscillator equation, from which the natural frequency is derived as

$$\omega_0 = \sqrt{\frac{3p_{l0}}{\rho R_0^2} + \frac{4\gamma}{\rho R_0^3} + \frac{12G_s}{\rho R_0^3}}, \tag{25}$$

where the initial pressure inside the bubble is replaced by the initial pressure at the liquid side by the initial equilibrium,

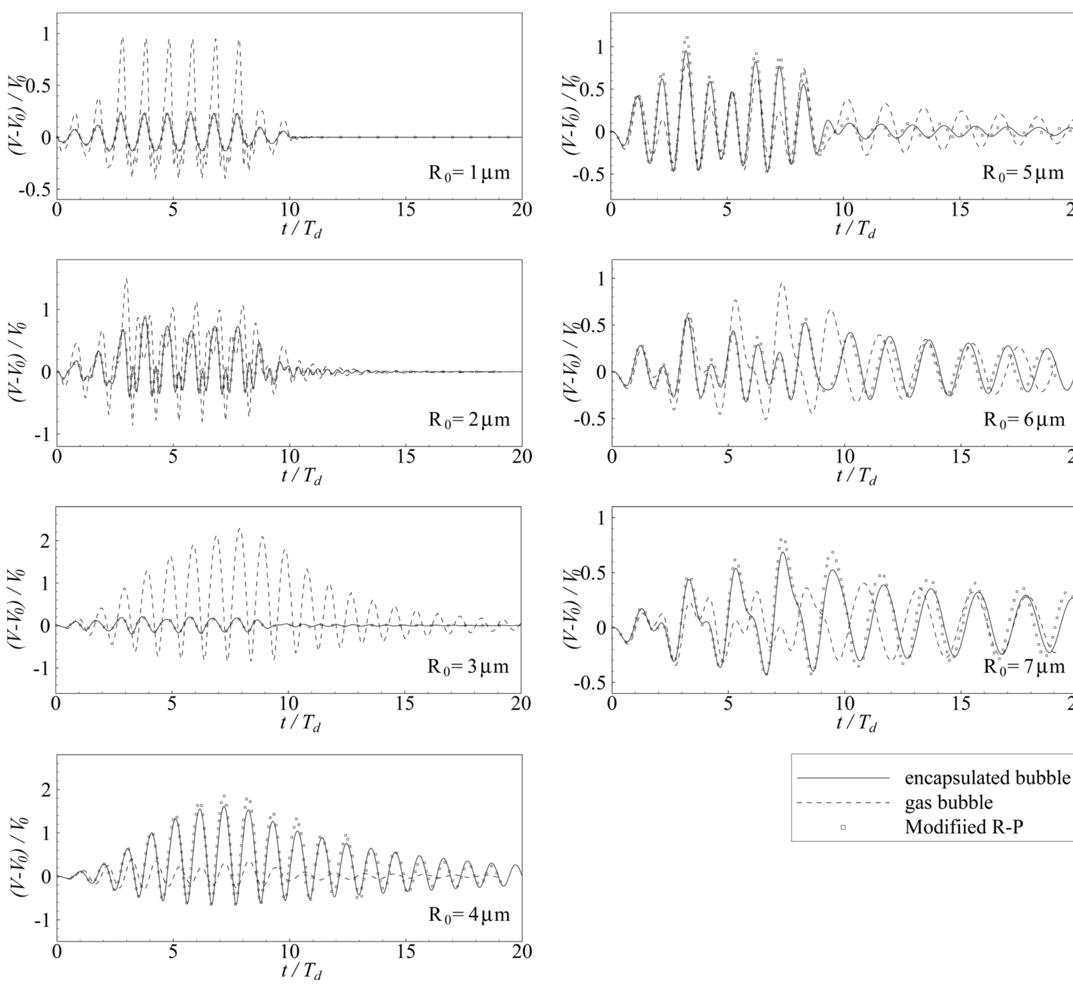

FIG. 9. Change rate of volume vs time for encapsulated bubbles (solid line), compared with the results of gas bubbles (dashed line), and the solutions to the modified Rayleigh–Plesset equation (square symbol).

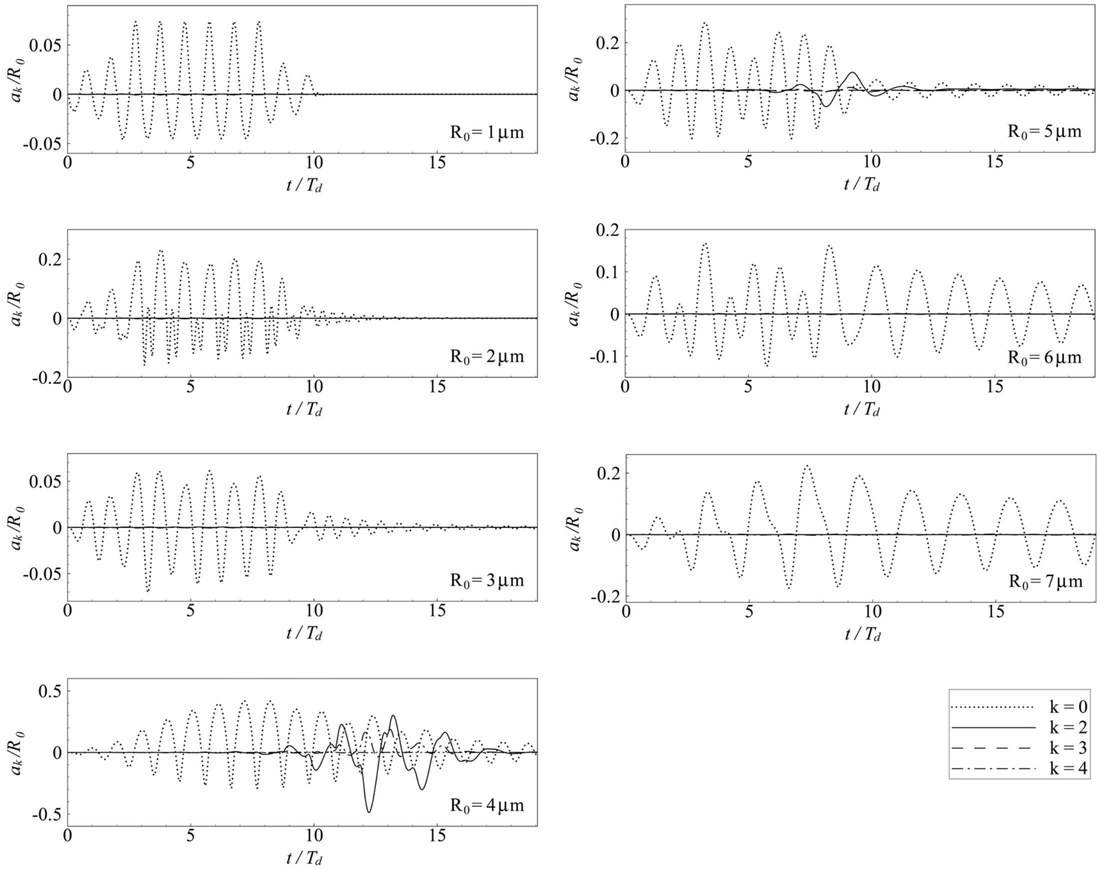

FIG. 10. Amplitudes of different modes vs time for encapsulated bubbles. Dotted line: $k=0$; solid line: $k=2$; dashed line: $k=3$; and dashed-dotted line: $k=4$.

$$p_{g0}=p_{l0}+\frac{2\gamma}{R_0}. \tag{26}$$

For encapsulated bubble, the surface tension term is ignored and the surface elastic modulus $G_s=0.1$ N/m. For gas bubble, the surface tension γ is set to be the gas-water tension of 0.0729 N/m and the surface elastic modulus G_s is equal to 0. The curves of natural frequency versus equilibrium radius for encapsulated and gas bubbles are plotted in Fig. 8. This figure stresses the fact that the natural frequency of an encapsulated bubble is higher than that of a gas bubble with the same size, especially for small bubbles, whereas the disparity is narrowing as the bubble radius increases.

The temporal variations of volume are shown in Fig. 9. Our computational results of encapsulated bubbles (solid line) are compared with those of gas bubbles (dashed line) and the Runge–Kutta solutions to the modified Rayleigh–Plesset equation [Eq. (23)] (square symbol). In the case of $R_0=1$ μm, the natural frequency of encapsulated bubble is approximately twice of that of gas bubble and six times of the driving frequency (1 MHz). The significant deviation of natural frequency from driving frequency results in the smaller oscillatory amplitude of encapsulated bubble. During contracting, the gas bubble presents higher harmonics. This phenomenon of strong nonlinearity comes from the large-amplitude pulsation. Actually, when the gas bubble contracts to the minimum size, the surface tension is quite strong due to its reciprocal relationship with radius. The resultant direction of surface tension always points inward the bubble. On the other hand, the pressure inside the bubble is also strong due to the smallest volume and directs outward from the bubble. These two strong but antidirectional forces compete with each other and cause the instability of higher harmonics. Concerning encapsulated bubble, on the other hand, the normal component of membrane stress does not necessarily direct toward the inside of bubble. Referred to Eqs. (12) and (15), F_n can be taken as either positive or negative, unlike the surface tension term $\gamma(\kappa_s+\kappa_\phi)$ which is absolutely positive. When the bubble contracts, the membrane experiences a compressive stress whose resultant direction is the same as that of internal pressure. Without the competition between two antidirectional forces and, of course, mainly due to the discrepancy in natural and driving frequencies, the encapsulated bubble oscillates in a stable manner. For a bigger bubble, such as $R_0=2$ μm, the oscillatory amplitude of encapsulated bubble is only slightly larger than that of gas bubble, as the two curves in Fig. 9 get closer and both of them approach to the driving frequency of 1 MHz. It is found that higher harmonics of the second order take place in both bubbles since either of their natural frequencies is in the upper or lower neighborhood of 2 MHz, twice of the driving frequency. Under driving frequency of 1 MHz, the resonant radius is in the vicinity of 3 μm for a gas bubble or 4 μm for an encapsulated bubble. These resonance phenomena are also revealed in Fig. 9. For $R_0=3$ μm, the gas bubble is at

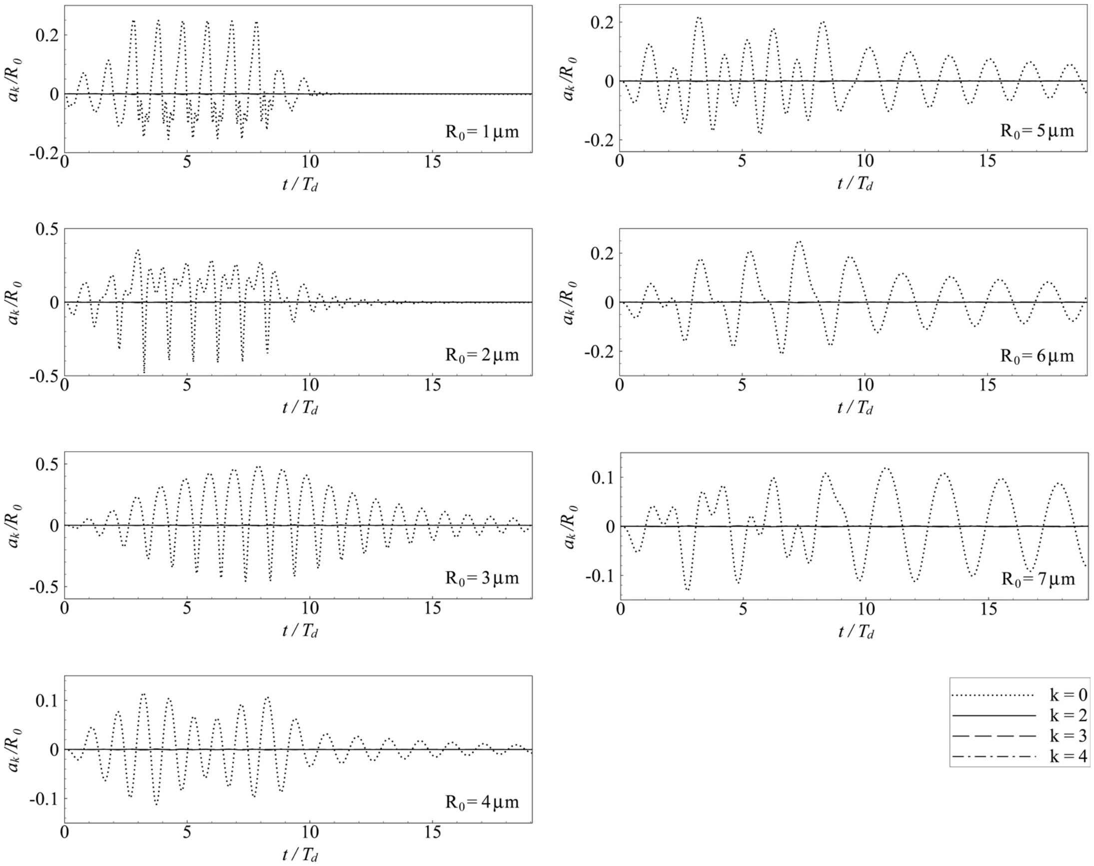

FIG. 11. Amplitudes of different modes vs time for gas bubbles. Dotted line: $k=0$; solid line: $k=2$; dashed line: $k=3$; and dashed-dotted line: $k=4$.

resonance. Therefore, the oscillatory amplitude keeps growing until the driving pressure stops. A similar phenomenon appears in the encapsulated bubble of $R_0=4\ \mu$m. In the following, we will show that the encapsulated bubble may become more unstable under resonance. For $R_0>5\ \mu$m, the difference in the amplitude of oscillation between gas and encapsulated bubbles further decreases, resulting from the fairly small difference in natural frequencies as shown in Fig. 8. At the same time, we find a subharmonic oscillation in a gas bubble of $R_0=6\ \mu$m, and the phenomenon occurs for an encapsulated bubble $R_0=7\ \mu$m. This can be again explained by Fig. 8. At driving frequency $\omega_d=2\pi\times 1$ MHz, ω_0 is equal to $\frac{1}{2}\omega_d$ at $R_0\approx 6\ \mu$m for a gas bubble and $R_0\approx 7\ \mu$m for an encapsulated bubble. It is known that subharmonic oscillation is easier to be induced when the driving frequency is twice of the natural frequency. In a word, it is the relationship between zeroth-order natural frequency and driving frequency that determine the radial oscillations of bubbles. The encapsulating membrane influences the behavior of a bubble through changing its natural frequency.

The radial mode $k=0$ and the shape modes from $k=2$ to $k=4$ are analyzed in terms of spherical harmonics. The evolutions of various modes for encapsulated and gas bubbles are plotted in Figs. 10 and 11, respectively. Obvious deformations occur in encapsulated bubble of $R_0=4\ \mu$m and $R_0=5\ \mu$m. In particular, in the case of $R_0=4\ \mu$m, where its natural frequency approaches to the driving frequency, the bubble becomes most unstable. The even order shape modes emerge after several intense pulsation cycles and oscillate in subharmonics. The second-order mode overwhelms the basic radial mode. The oblate and prolate shapes appear alternatively (Fig. 12). To validate whether the shape deformation originates from numerical instability, we calculate the kinetic energy budget and confirm that the system is conserved during simulation, the detail of which is presented in the Appen-

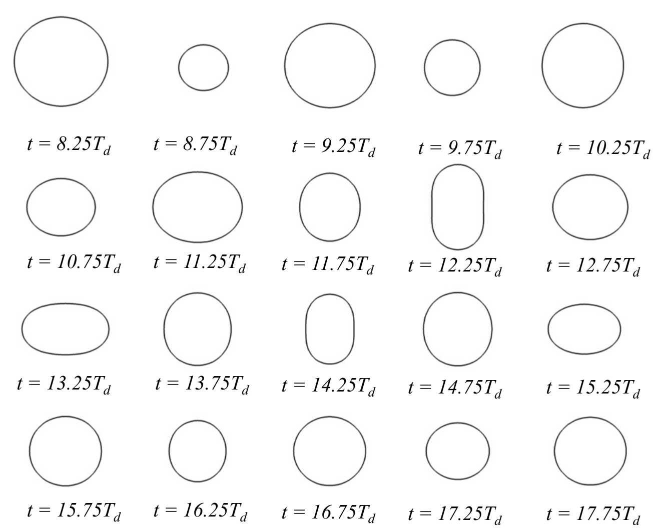

FIG. 12. Instantaneous shapes of an encapsulated bubble ($R_0=4\ \mu$m) from $t=8.25T_d$ to $t=17.75T_d$ with interval of $0.5T_d$.

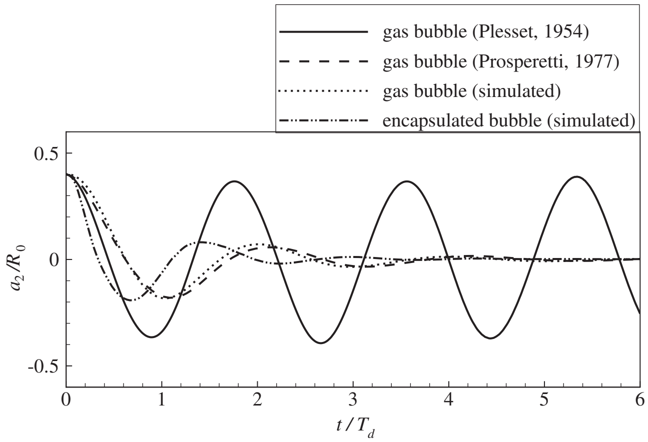

FIG. 13. Amplitudes of the second-order shape mode vs time during free oscillations of bubbles ($R_0=4$ μm).

dix. On the other hand, for gas bubble, even at comparable pulsation amplitude concerning the resonant state of $R_0=3$ μm, the bubble remains spherical, i.e., only the zeroth-order mode exists.

To further understand the mechanism responsible for the onset of shape oscillations, we investigate the natural frequencies of shape modes. It is well known that for gas bubble, the natural frequency of the kth-order mode is[31]

$$\omega_k^{gas} = \sqrt{(k-1)(k+1)(k+2)\frac{\gamma}{\rho R_0^2}}. \tag{27}$$

However, this natural frequency does not involve the effect of membrane. Since there is no available formula to calculate the higher-order natural frequency of an encapsulated bubble up to date, we here evaluate it through simulating its free oscillation. If we impose an initial disturbance to a specific shape mode and do not apply any driving, the shape mode will damp at its own natural frequency. Only the second-order natural frequency is discussed here because we found that this mode is dominant in the above simulation. Here we present an example of $R_0=4$ μm in Fig. 13 to illustrate the temporal variation of the second-order amplitude a_2, in which a disturbance of $0.4R_0$ is given initially. We first solve the following differential equation for the amplitude of shape mode of a gas bubble (derived by Plesset[3]):

$$\ddot{a}_k + \frac{3\dot{R}}{R}\dot{a}_k + (k-1)\left[-\frac{\ddot{R}}{R} + (k+1)(k+2)\frac{\gamma}{\rho R^3}\right]a_k = 0 \tag{28}$$

along with the Rayleigh–Plesset equation by means of the fourth-order Runge–Kutta method. It is noted that the coefficient before a_k represents the natural frequency and is consistent with Eq. (27) if the transient term is dropped. The solution to Eq. (28) is plotted out in solid line in Fig. 13. Measuring the distance of two consecutive wave troughs, we obtain the natural period and then natural frequency. The natural frequencies from numerically solving Plesset's equation [Eq. (28)] are recorded in Table I. They are identical to those obtained in Eq. (27), implying the rationality of the method to obtain natural frequency through simulating bubble's free oscillation. However, when we simulate the free oscillations of gas bubbles using our DNS code, we find large errors ($>10\%$) with those obtained in Eq. (28). It is known that Eq. (28) eliminates the effect of viscosity. To investigate how much the viscous effect will influence the natural frequency, we solve Prosperetti's model,[32] in which the viscous effect is taken into account in terms of vorticity. The differences in natural frequencies obtained by Prosperetti's model and our DNS are greatly reduced (see the third and fourth rows in Table I and the dashed and dotted lines in Fig. 13), which means the viscosity actually influences the natural frequency and, furthermore, the method to evaluate the natural frequency through simulating free oscillation by our code is reasonable. We thereby evaluate the higher-order natural frequencies of encapsulated bubbles, recorded in Table I and one example of $R_0=4$ μm shown in dashed-dotted line in Fig. 13.

The data in Table I reveal that, similar to the radial mode, the natural frequencies of shape mode are greatly different between gas and encapsulated bubbles for small size, while this discrepancy narrows as the bubbles become bigger. The most interesting is that the second-order natural frequencies of encapsulated bubbles are in the neighborhood of half of the driving frequency (1 MHz) at $R_0=4$ μm and $R_0=5$ μm, i.e., $\omega_d \approx 2\omega_2$. This is the most unstable situation under which the resonance interaction between radial and shape oscillations satisfies, leading to the emergence of higher-order shape mode. This is the so-called parametric

TABLE I. Natural frequencies of gas bubbles and encapsulated bubbles.

R_0 (μm)	1	2	3	4	5	6	7
ω_2^{gas} ($2\pi\times$MHz) [a]	4.71	1.66	0.91	0.59	0.42	0.32	0.25
ω_2^{gas} ($2\pi\times$MHz) [b]	4.63	1.67	0.91	0.59	0.42	0.32	0.25
ω_2^{gas} ($2\pi\times$MHz) [c]	2.78	1.20	0.72	0.49	0.35	0.26	0.21
ω_2^{gas} ($2\pi\times$MHz) [d]	3.50	1.37	0.79	0.51	0.36	0.28	0.22
ω_2^{encap} ($2\pi\times$MHz) [d]	10.53	3.14	1.27	0.64	0.44	0.33	0.27

[a]Reference 31.
[b]Reference 3.
[c]Reference 32.
[d]Simulated.

TABLE II. Four cases for simulation, where cases a and d and cases b and c have the same resonance frequencies.

	a	b	c	d
G_s (N/m)	0	0.1	0	0.0243
γ (kg/s^2)	0.0729	0	0.3	0
ω_0 ($2\pi\times$MHz)	0.77	0.97	0.97	0.77
ω_2 ($2\pi\times$MHz)	0.51	0.64	2.78	0.33

instability which has been widely discussed for gas bubble, such as in the papers we reviewed in Sec. I. The above simulations reveal that this condition also holds for encapsulated bubble. The analysis in the view of resonance interaction validates the above results of simulation that the encapsulated bubble tends to deform around $R_0=4$ μm and $R_0=5$ μm. Moreover, the twice multiple relationship between ω_d and ω_2 sheds light on the subharmonic characteristic in shape oscillation. The gas bubble, although satisfying the relationship $\omega_d \approx 2\omega_2$ at $R_0=4$ μm, does not experience shape oscillation. The reason is that parametric instability requires an excitation by radial pulsation when the radial amplitude is above a certain critical value.[5] The gas bubble of $R_0=4$ μm is out of radial resonance with respect to the driving frequency of 1 MHz, and thus the radial pulsation is not large enough to induce the surface instability. In addition, surface tension is strong when the bubble is small, say for that at the order of 1 μm. The study by Hilgenfeldt *et al.*[33] predicted that an extremely high forcing pressure amplitude (1.2–1.5 atm) is needed to induce shape instability in gas bubble at $R_0 \approx 4-5$ μm. While at $R_0=3$ μm when the gas bubble is at radial resonance, the relationship $\omega_d \approx 2\omega_2$ does not hold; hence, the shape oscillation still does not take place.

According to Eq. (25), if the surface tension of a gas bubble is chosen to be 0.3 N/m, its natural frequency is equal to that of an encapsulated bubble with surface elastic modulus of 0.1 N/m. In this case, the resonance curve is over-

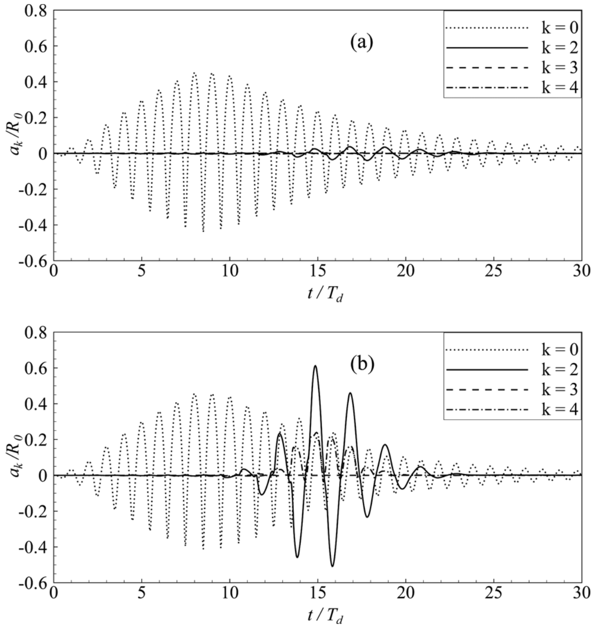

FIG. 15. Development of shape modes for (a) a gas bubble with $\gamma=0.04$ N/m and (b) an encapsulated with $G_s=0.013$ N/m.

lapped with that of the encapsulated bubble in Fig. 8. Similarly, we can set the surface elastic modulus to be 0.0243 N/m so that its natural frequency is equal to that of the gas bubble with surface tension of 0.0729 N/m. The above-mentioned cases, together with the normal gas bubble and encapsulated bubble cases, and their respective natural frequencies at zeroth and second orders are listed in Table II, where cases a and d and cases b and c have the same natural frequencies of radial mode, respectively. From the developments of different modes (Fig. 14), we find that the volume oscillations ($k=0$) behave in a similar manner for those with the same radial natural frequency. However, deformation only emerges in case b. The gas bubble of case c keeps spherical even it has a comparable pulsation amplitude with

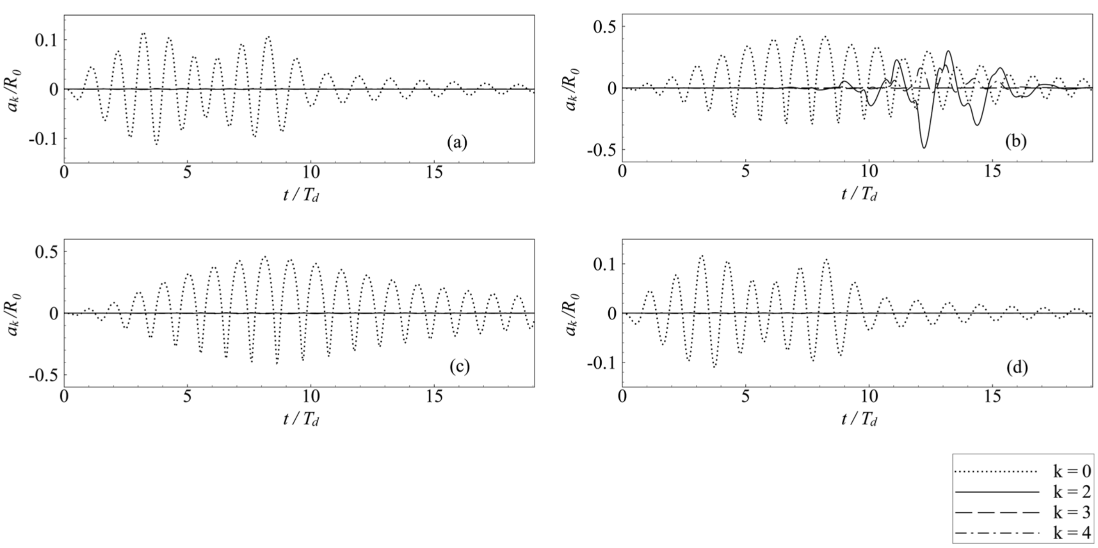

FIG. 14. Development of shape modes for the four cases listed in Table II ($R_0=4$ μm). Cases a and d and Cases b and c have the same resonance frequencies, respectively.

case b because the second-order natural frequency of case c is much higher than its zeroth-order frequency, and thus the resonance relationship does not satisfy. For case d, although it is an encapsulated bubble without the stabilizing effects of surface tension and although the second-order natural frequency is not far from half of its zeroth-order frequency, the radial amplitude is not large enough to induce the shape mode.

It is noted that the parameters for the gas and encapsulated bubble we chose above are specific. Actually, it is not the values themselves but the relationship among natural frequencies of different orders that determines the surface stability of a bubble. To prove this viewpoint, we choose a smaller surface tension for gas bubble of 0.04 N/m, which is related to a bubble contaminated by surfactant. For this surface tension, the bubble with initial radius of $R_0=6\ \mu$m happens to satisfy the relationship of $\omega_0 \approx 2\omega_2$. On the other hand, we set the elastic modulus of an encapsulated bubble as 0.013 N/m to let it have the same natural frequencies at zeroth and second orders as those of the gas bubble. In other words, for both the gas and encapsulated bubbles with initial radii $R_0=6\ \mu$m, their radial and second-order natural frequencies are approximately equal, respectively, where $\omega_0 = 2\pi \times 0.48$ MHz and $\omega_2 = 2\pi \times 0.23$ MHz. Here, the natural frequencies are evaluated by our simulations on free oscillations. We drive both of the bubbles at their radial natural frequency: $\omega_d = 2\pi \times 0.48$ MHz. As shown in Fig. 15, the two bubbles oscillate in a similar radial oscillation, which ensures that the relationship between radial natural frequency and driving frequency determines the manner of radial oscillation. Moreover, the second-order shape mode happens in both of them, which means the integer multiple relationship between second-order natural frequency and radial frequency of $\omega_0 (=\omega_d) \approx 2\omega_2$ is the key point to induce second-order shape mode, no matter for gas bubble or encapsulated bubble. However, we find that the second-order amplitude in encapsulated bubble is larger than that in gas bubble. This can be explained in terms of the directions of surface tension and membrane stress. Surface tension is always positive and its effect is to keep the bubble in the most stably spherical shape. For encapsulated bubble, the membrane stress [F_n in Eq. (12)] is not necessarily positive. The negative F_n implies a compressive stress. The membrane stressed under compression becomes unstable by a mechanism of the Euler buckling.[34]

IV. CONCLUSIONS

We numerically investigated the dynamics of an encapsulated bubble in the ultrasound field. The mass conservation and the Navier–Stokes equation were directly solved to obtain the flow field. The basic equations were discretized on a boundary-fitted grid in order to accurately capture the shape of bubble. The dynamics of bubble surface was controlled by the traction jump equation coupled with membrane mechanics. In this study, we chose the neo-Hookean model as a constitutive law to relate the in-plane stress to the finite surface deformation.

The numerical methods were validated through simulating the shape oscillation of a gas bubble driven by an applied pressure pulse. The results are consistent with experimental results. Subsequently, a bubble encapsulated by a neo-Hookean membrane was investigated. The results were compared with those of gas bubbles to investigate the effect of membrane. In the case of small bubble, e.g., $R_0=1\ \mu$m, the oscillation of an encapsulated bubble is more stable than that of a gas bubble since the membrane increases the natural frequency, which is greatly higher than the driving frequency. At the same time, the membrane stress restrains the higher harmonics which emerges in gas bubble of the same size during contracting. As the bubble size increases, the discrepancy in natural frequency between gas and encapsulated bubbles narrows, leading to the reduction of the difference in oscillatory amplitude. Shape oscillations take place when the natural frequencies of the second-order shape mode and the radial mode have an integer multiple relationship, i.e., $\omega_d \approx 2\omega_2$. Especially at radial resonance ($\omega_d \approx \omega_0$), the large-amplitude pulsation enhances the surface instability and thus the deformation becomes significant. Under the same resonance relationship, namely, $\omega_0 \approx 2\omega_2$ and $\omega_d \approx \omega_0$, the encapsulated bubble experiences a more obvious shape oscillation than the gas bubble. This phenomenon is related to the different stresses developing at the interfaces of encapsulated

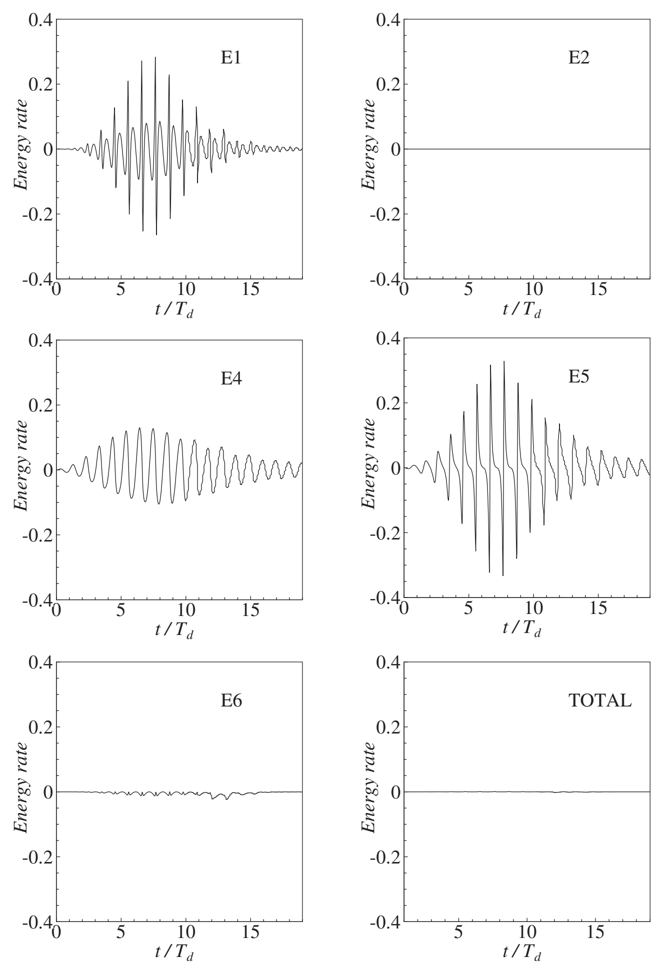

FIG. 16. Energy budget for an encapsulated bubble ($R_0=4\ \mu$m). The last figure reveals the total energy.

and gas bubbles. For the encapsulated bubble, the membrane bears a compressive stress which leads to the buckling instability, while for the gas bubble, the surface tension always tries to keep the interface in a spherical shape.

ACKNOWLEDGMENTS

We thank Huaxiong Huang for fruitful discussion. This work was supported by the Japanese Government Scholarship (Grant No. 073138) of the Ministry of Education, Culture, Sports, Science and Technology (MEXT) and by the Grant-in-Aid for Young Scientist (B) (Grant No. 21760120) of MEXT.

APPENDIX: ENERGY BUDGET

To validate whether the deformation in encapsulated bubble is from any numerical source, we compute the budget of kinetic energy transport. If the cause was due to an aliasing error leading to numerical instability, a spurious energy would be introduced into the system, and the budget would be violated. The overall energy dissipation equation is derived by the dot product of the Navier–Stokes equation [Eq. (3)] with the velocity. Here we express it in the vector form,

$$\begin{aligned}E_{total} = &\underbrace{-\frac{\partial}{\partial t}\int_{\Omega} K dV}_{\text{E1}} \underbrace{- \int_{\partial\Omega_f} \mathbf{n}\cdot(\mathbf{u}K)dS}_{\text{E2}} \\ &\underbrace{+ \int_{\partial\Omega_b} \mathbf{n}\cdot(\mathbf{u}K)dS}_{\text{E3}} \underbrace{+ \int_{\partial\Omega_f} \mathbf{n}\cdot(\mathbf{u}\cdot\boldsymbol{\sigma})dS}_{\text{E4}} \\ &\underbrace{- \int_{\partial\Omega_b} \mathbf{n}\cdot(\mathbf{u}\cdot\boldsymbol{\sigma})dS}_{\text{E5}} \underbrace{- 2\mu\int_{\Omega} \mathbf{E}:\mathbf{E}dV}_{\text{E6}},\end{aligned} \tag{A1}$$

where $K[=\frac{1}{2}\rho(\mathbf{u}\cdot\mathbf{u})]$ is the kinetic energy, $\boldsymbol{\sigma}(=-p\mathbf{I}+2\mu\mathbf{E})$ is the stress tensor, and $\mathbf{E}[=\frac{1}{2}(\nabla\mathbf{u}+\nabla\mathbf{u}^{\mathrm{T}})]$ is the rate-of-strain tensor. In Eq. (A1), Ω denotes the whole computational domain and $\partial\Omega$ is its boundary with the subscript f denoting the far field boundary and b denoting the bubble surface. The total energy dissipation includes the time derivative of kinetic energy (E1), the energy flux due to mass transfer in the far field (E2) and at the bubble surface (E3), the energy flux owing to internal friction in the far field (E4) and at the bubble surface (E5), and the viscous dissipation rate (E6). An example for the case of $R_0=4$ μm with the largest deformation is shown in Fig. 16, including the temporal variation of each term. It is noted that the bubble interface moves at the boundary velocity; thus, the mass transfer and then the energy flux (E3) at the bubble surface are zero. For this reason, we do not plot it out. E2 is also small since we choose the computational domain large enough to eliminate the boundary effect and promise the velocity in the far field small. Consequently, the time derivative of kinetic energy, the energy flux due to internal friction, and the viscous dissipation compensate with each other. The absolute value of the total energy E_{total}, corresponding to the numerical error, is less than 0.001, which is much smaller than the variation of the contributions of the individual terms. In view of the energy balance, the system is well conserved during the simulation. The examination of energy budget excludes the possibility of numerical instability in our simulations.

[1] J. R. Lindner, "Microbubbles in medical imaging: Current applications and future directions," Nat. Rev. Drug Discovery **3**, 527 (2004).
[2] E. C. Unger, E. Hersh, M. Vannan, T. O. Matsunaga, and T. McCreery, "Local drug and gene delivery through microbubbles," Prog. Cardiovasc. Dis. **44**, 45 (2001).
[3] M. S. Plesset, "On the stability of fluid flows with spherical symmetry," J. Appl. Phys. **25**, 96 (1954).
[4] T. B. Benjamin, "Surface effects in non-spherical motions of small cavities," in *Cavitation in Real Liquids*, edited by R. Davies (Elsevier, New York, 1964), pp. 164–180.
[5] A. Francescutto and R. Nabergoj, "Pulsation amplitude threshold for surface waves on oscillating bubbles," Acustica **41**, 215 (1978).
[6] S. M. Yang, Z. C. Feng, and L. G. Leal, "Nonlinear effects in the dynamics of shape and volume oscillations for a gas bubble in an external flow," J. Fluid Mech. **247**, 417 (1993).
[7] Z. C. Feng and L. G. Leal, "On energy transfer in resonant bubble oscillations," Phys. Fluids A **5**, 826 (1993).
[8] N. K. McDougald and L. G. Leal, "Numerical study of the oscillations of a non-spherical bubble in an inviscid, incompressible liquid. Part I: Free oscillations from non-equilibrium initial conditions," Int. J. Multiphase Flow **25**, 887 (1999).
[9] N. K. McDougald and L. G. Leal, "Numerical study of the oscillations of a non-spherical bubble in an inviscid, incompressible liquid. Part II: The response to an impulsive decrease in pressure," Int. J. Multiphase Flow **25**, 921 (1999).
[10] N. de Jong, R. Cornet, and C. T. Lancée, "Higher harmonics of vibrating gas-filled microspheres. Part one: Simulations," Ultrasonics **32**, 447 (1994).
[11] C. C. Church, "The effects of an elastic solid surface layer on the radial pulsations of gas bubbles," J. Acoust. Soc. Am. **97**, 1510 (1995).
[12] L. Hoff, P. C. Sontum, and J. M. Hovem, "Oscillations of polymeric microbubbles: Effect of the encapsulating shell," J. Acoust. Soc. Am. **107**, 2272 (2000).
[13] K. E. Morgan, J. S. Allen, P. A. Dayton, J. E. Chomas, A. L. Klibaov, and K. W. Ferrara, "Experimental and theoretical evaluation of microbubble behavior: Effect of transmitted phase and bubble size," IEEE Trans. Ultrason. Ferroelectr. Freq. Control **47**, 1494 (2000).
[14] D. Y. Hsieh and M. S. Plesset, "Theory of rectified diffusion of mass into gas bubbles," J. Acoust. Soc. Am. **33**, 206 (1961).
[15] A. E. Green and J. E. Adkins, *Large Elastic Deformations and Non-Linear Continuum Mechanics* (Clarendon, Oxford, 1960).
[16] D. Barthès-Biesel and J. M. Rallison, "The time-dependent deformation of a capsule freely suspended in a linear shear flow," J. Fluid Mech. **113**, 251 (1981).
[17] C. Quéguiner and D. Barthès-Biesel, "Axisymmetric motion of capsules through cylindrical channels," J. Fluid Mech. **348**, 349 (1997).
[18] A. Diaz, N. Pelekasis, and D. Barthès-Biesel, "Transient response of a capsule subjected to varying flow conditions: Effect of internal fluid viscosity and membrane elasticity," Phys. Fluids **12**, 948 (2000).
[19] S. Ramanujan and C. Pozrikidis, "Deformation of liquid capsules enclosed by elastic membranes in simple shear flow: Large deformations and the effect of fluid viscosities," J. Fluid Mech. **361**, 117 (1998).
[20] C. Pozrikidis, "Deformed shapes of axisymmetric capsules enclosed by elastic membranes," J. Eng. Math. **45**, 169 (2003).
[21] M. Versluis, D. E. Goertz, P. Palanchon, I. L. Heitman, S. M. van der Meer, B. Dollet, N. de Jong, and D. Lohse, "Microbubble shape oscillations excited through ultrasonic parametric driving," Phys. Rev. E **82**, 026321 (2010).
[22] S. Takagi, A. Prosperetti, and Y. Matsumoto, "Drag coefficient of a gas bubble in an axisymmetric shear flow," Phys. Fluids **6**, 3186 (1994).
[23] S. Takagi, Y. Matsumoto, and H. Huang, "Numerical analysis of a single rising bubble using boundary-fitted coordinate system," JSME Int. J., Ser. B **40**, 42 (1997).
[24] A. Prosperetti, L. A. Crum, and K. W. Commander, "Nonlinear bubble dynamics," J. Acoust. Soc. Am. **83**, 502 (1988).
[25] M. S. Plesset and D. Y. Hsieh, "Theory of gas bubble dynamics in oscillating pressure fields," Phys. Fluids **3**, 882 (1960).

[26] A. Prosperetti, "The thermal behaviour of oscillating gas bubbles," J. Fluid Mech. **222**, 587 (1991).
[27] R. Skalak, A. Tozeren, R. P. Zarda, and S. Chien, "Strain energy function of red blood cell membranes," Biophys. J. **13**, 245 (1973).
[28] M. Mooney, "A theory of large elastic deformation," J. Appl. Phys. **11**, 582 (1940).
[29] K. Sarkar, W. T. Shi, D. Chatterjee, and F. Forsberg, "Characterization of ultrasound contrast microbubbles using in vitro experiments and viscous and viscoelastic interface models for encapsulation," J. Acoust. Soc. Am. **118**, 539 (2005).
[30] C. Pozrikidis, "The axisymmetric deformation of a red blood cell in uniaxial straining Stokes flow," J. Fluid Mech. **216**, 231 (1990).
[31] H. Lamb, *Hydrodynamics* (Cambridge University Press, Cambridge, 1932).
[32] A. Prosperetti, "Viscous effects on perturbed spherical flows," Q. Appl. Math. **34**, 339 (1977).
[33] S. Hilgenfeldt, D. Lohse, and M. Brenner, "Phase diagrams for sonoluminescing bubbles," Phys. Fluids **8**, 2808 (1996).
[34] D. O. Brush and B. O. Almroth, *Buckling of Bars, Plates, and Shells* (McGraw-Hill New York, 1975), Vol. 6.